arXiv:2606.28529v2 [cs.RO] 30 Jun 2026

The Speedup Paradox: Rethinking Inference Speed-Quality Trade-off in Embodied Tasks

Yujin Wang **Junli Chen** **Yixuan Li** **Shunan Dong**
Huazhong Yang **Yongpan Liu** **Hongyang Jia**
Tsinghua University
yujin-wa24@mails.tsinghua.edu.cn hjia@tsinghua.edu.cn

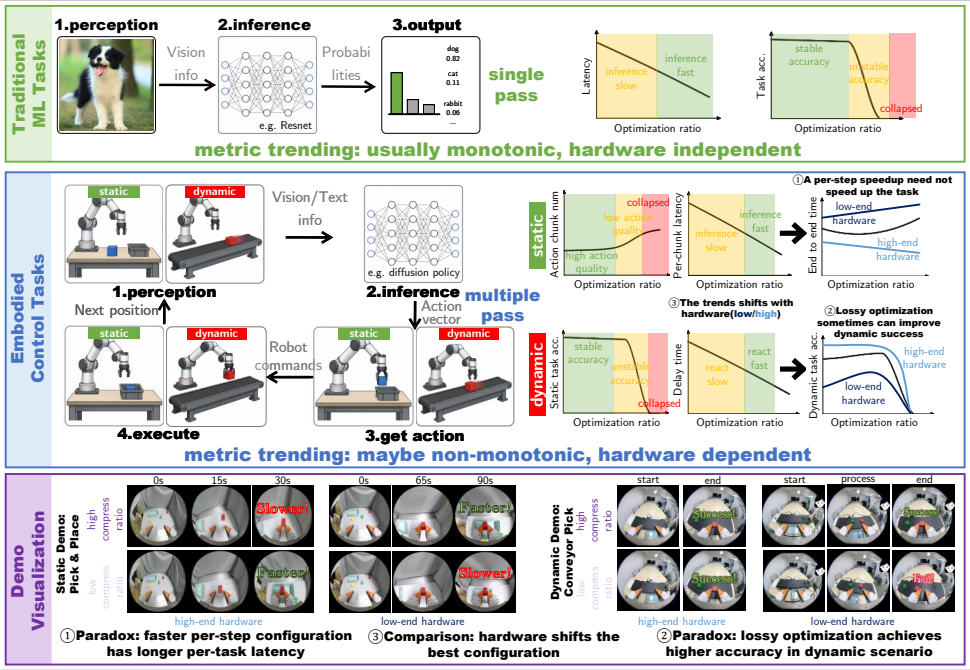

Figure 1: Overview of the speed-quality trade-off in embodied inference. Unlike static ML tasks, where stronger lossy optimization monotonically trades accuracy for per-step speed, lightweighting embodied policies yields non-monotonic task-level behavior: both end-to-end completion time (static tasks) and task success rate (dynamic tasks) may exhibit a sweet spot, whose location further shifts with the deployment hardware.

Abstract: Embodied foundation models have recently been widely used to improve robot generalization and task success rates. Previous works apply lossy efficient-inference techniques such as quantization, pruning, and asynchronous inference, accepting small action quality degradation in exchange for lower per-step computation cost and inter-action latency. However, unlike traditional static ML tasks, embodied tasks involve repeated interaction with the environment, and task-level performance is determined not only by per-step cost, but also by closed-loop effects unique to embodied execution, which remain insufficiently characterized in current efficient-inference studies. In this work, we propose TISED (Task-level Inference Speedup Effect Decomposition), an analytical framework that unifies diverse lossy inference optimization techniques and decomposes their effects on static and dynamic tasks, and uncovers some paradoxical effects on task-level performance: (1) on *static tasks*, optimization sometimes can lengthen end-to-end per-task completion time even as per-step latency drops; (2) on *dynamic tasks*, moderate lossy optimization can raise task success rate even above the baseline; and (3) the monotonicity and sweet-spot location of both effects can shift with hardware configuration. Together, our findings provide a new perspective on adapting inference optimization techniques to embodied tasks.

Keywords: Embodied Tasks, Lightweight, Quantization, Pruning, Hardware-Software Co-design, Asynchronous Inference.

1 Introduction

Embodied models such as Vision-Language-Action models (VLA) [1, 2, 3, 4, 5, 6, 7, 8] and World-Action Models (WAM) [9, 10, 11, 12] have been widely deployed across diverse embodied scenarios. These models are typically obtained by fine-tuning large-scale pretrained vision-language models [13, 14] and world models [15, 16], yielding strong cross-task generalization and improved robustness to environmental variation. However, to fully accommodate these capabilities, they usually have large parameter counts and compute FLOPs at inference time, posing a key barrier to edge deployment and real-time control.

To address this, many recent works apply lossy inference optimization techniques to embodied models, such as quantization [17, 18], cache reuse [19, 20, 21], sampling step reduction [22, 23, 24], and asynchronous scheduling [25, 26, 27]. These methods have been shown to reduce per-step inference latency or shorten the gap between consecutive action chunks with slight accuracy degradation. Embodied tasks, however, differ fundamentally: Each cycle of the inference-execution loop consists of one policy inference and the subsequent action execution, and the loop runs for many such cycles before a rollout terminates. The per-step latency reductions from these methods therefore capture only a fragment of task-level performance: they ignore how many cycles the rollout ultimately requires until success, how the environment evolves during model inference, and how all of these interact with hardware performance across inference and execution costs.

To analyze how lossy inference optimization shapes embodied task performance beyond per-step latency, we propose TISED (Task-level Inference Speedup Effect Decomposition) analysis in Figure 1. First, we place policy-intrinsic and execution-aware optimization on a common per-chunk time formula. Building on this unified view, we model the end-to-end objective separately for the two task regimes: on static tasks, end-to-end completion time is jointly determined by the per-chunk inference time and the number of chunks that the full rollout requires; on dynamic tasks, task success rate is jointly determined by action quality and observation staleness.

We empirically test these predictions with a progressive-lightweighting sweep across task types, model backbones, optimization methods, and compute platforms, from which three observations emerge: **(1)** On static tasks, end-to-end completion time is sometimes *non-monotonic* in the lightweighting strength due to the deterioration of action quality (per-step inference latency reduction $\neq$ end-to-end per-task latency reduction). **(2)** On dynamic tasks, task success rate is sometimes *non-monotonic* in the lossy optimization strength due to the trade-off between degraded action quality and reduced observation staleness (static task accuracy $\neq$ dynamic task accuracy). **(3)** Fixing the task and lightweighting method, the above trends and the location of the sweet spot shifts with the hardware compute budget. Together, these three observations show that the per-step speed-quality trade-off familiar from static ML no longer predicts task-level outcomes in embodied closed-loop execution—speed and quality interact through rollout length, action delay, and hardware budget.

2 Related Works

2.1 Embodied Foundation Models

Recent progress in vision-language-action models (VLA) [1, 2, 3, 4, 5, 6, 7, 8] and world-action models (WAM) [9, 10, 11, 12] have enabled stronger open-world generalization, task adaptation, and large-scale policy transfer. However, these capabilities come at a high inference cost. For example, by default π_0 [3] (3.3B parameters) is deployed on high-end consumer GPUs such as RTX 4090, and Cosmos-Policy [9] (2B parameters) on datacenter-class accelerators such as H100. This is a key barrier to edge deployment and low-latency control. In this work, rather than scaling capabilities or enhancing generalization, we study how to deploy these models efficiently in the inference-execution loop.

2.2 Lossy Optimizations for Embodied Model Inference

To reduce the computational burden of embodied models, recent work has explored a range of lossy lightweight inference strategies. These methods can be grouped into two categories: (1) *Policy-intrinsic optimization*, which reduces the cost of each forward pass through techniques such as quantization [17, 18, 28, 29], denoise step reduction [30, 31, 32, 33], and cache reuse [19, 20, 21, 34]. For example, Q-VLA [18] analyzes how different components of a VLA vary in quantization sensitivity and assigns mixed precision accordingly to minimize the resulting action error; VLA-Cache [19] exploits the sparsity of background visual information across perception steps and reuses less-salient tokens to reduce redundant computation. (2) *Execution-aware optimization*, which improves effective control frequency by overlapping inference with execution, such as asynchronous scheduling [25, 26, 27]. For example, VLASH [25] rolls the robot state forward using the previously generated action chunk to predict the state at execution time, and further reduces prediction-execution misalignment by fine-tuning. Most of these works focus only on reducing the latency of a single inference, leaving a systematic analysis of end-to-end effects in embodied scenarios largely unexplored. In this work, rather than targeting a specific lightweight algorithm, we provide a unified modeling framework to analyze the unique impact of such algorithms on embodied tasks.

2.3 Efficiency-Accuracy Trade-off Characterizations

Aggressive lossy optimization methods can achieve significant gains in latency or energy efficiency while harming the accuracy. Previous works such as Deep Compression [35] established a trade-off between efficiency and accuracy in deep learning models. Subsequently, a lot of research has attempted to push this Pareto frontier forward in vision and language models [36, 37, 38, 39, 40]. In embodied systems, this relationship becomes more complex due to error accumulation and closed-loop feedback. Works such as [41, 42] introduced a new trade-off between efficiency and accuracy in time-sensitive tasks, but their scope was limited to object detection or LLM agents. Works such as [34, 43, 44] have characterized the inference performance of VLA models across various hardware devices but lack task-level performance. Work [45] provides valuable analysis of the negative impact of model lightweighting on execution in embodied task scenarios, while their focus is on the negative side. In this work, we further explore the synergy between the positive and negative effects of lightweight optimization and conduct a cross-hardware study.

3 Task-Level Inference Speedup Effect Decomposition

Embodied inference optimization operates within an inference-execution loop, not during a single forward pass. Therefore, a per-step speedup does not translate directly into a task-level gain: it changes both how many control cycles a rollout needs and how stale the observation is when the resulting action is executed. These two effects give rise to different failure modes in different task regimes. We develop this view into TISED, which analyzes task-level performance across lightweighting strength, task dynamics, and hardware budget. TISED places policy-intrinsic and execution-aware optimization on a common closed-loop time axis, and separates the end-to-end effect into cycle time, rollout length, and action delay.

We use two task regimes throughout the paper. In a *static task*, the task-relevant environment state remains effectively unchanged during model inference (e.g., static pick & place task). In this regime, lightweighting primarily affects movement smoothness and total execution time. In a *dynamic task*, the task-relevant environment state evolves while the model is still computing the next action (e.g., picking a rolling ball or playing ping-pong). In this regime, lightweighting changes both action quality and reaction speed – the inference speed directly affects the policy's ability to react to dynamic environments. More detailed analysis and derivation can be found in Appendix A.

3.1 Basic Timing Model

As shown in Figure 2, let T_{inf} be the latency of one full-model policy inference, n the action chunk size [46], and T_{act} the duration of one action. In the synchronous full-model baseline, one chunk consists of one inference followed by n executed actions. We use this baseline chunk time as the reference cost:

$$T_{\text{chunk}} = T_{\text{inf}} + nT_{\text{act}}. \tag{1}$$

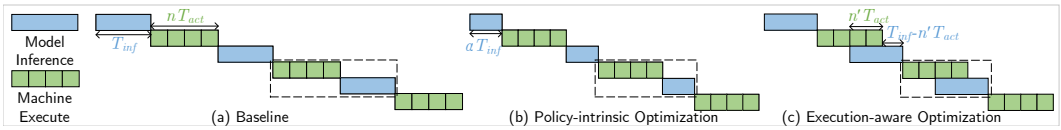

Figure 2: Dataflow of the inference-execution loop in different optimization settings. The black dashed box indicates the per-chunk latency.

Policy-Intrinsic Optimization. Policy-intrinsic methods reduce computation inside the policy network. We represent their timing effect by a latency ratio $\alpha \in (0, 1]$. This ratio can be changed by adjusting the number of quantization layers, the pruning ratio, and so on. Under this class of methods, the realized per-chunk time and per-chunk speedup are:

$$T^{\text{pl}}_{\text{cycle}}(\alpha) = \alpha T_{\text{inf}} + nT_{\text{act}}, \quad \eta^{\text{pl}}_{\text{chunk}}(\alpha) = \frac{T_{\text{chunk}}}{T^{\text{pl}}_{\text{cycle}}(\alpha)}. \tag{2}$$

The cost is that stronger lightweighting may reduce action quality.

Execution-Aware Optimization. Execution-aware methods like asynchronous inference change how inference is scheduled with robot execution, and they usually require complex system scheduling. To simplify the analysis, we performed abstract modeling of asynchronous inference by emulating work [25]. We summarize the scheduling knob by an action overlap depth $n' \in \{0, \ldots, n\}$, the number of primitive actions whose execution can overlap with the next inference. The realized per-chunk time and per-chunk speedup are:

$$T^{\text{ea}}_{\text{cycle}}(n') = T_{\text{inf}} + nT_{\text{act}} - \min\{T_{\text{inf}}, n'T_{\text{act}}\}, \quad \eta^{\text{ea}}_{\text{chunk}}(n') = \frac{T_{\text{chunk}}}{T^{\text{ea}}_{\text{cycle}}(n')}. \tag{3}$$

By overlapping the next inference with the current chunk's execution, each new action is computed from an observation taken before those actions complete, so the policy acts on an increasingly outdated view of the environment and also degrades the action quality.

3.2 Task-level Model

End-to-End Time. A complete embodied task spans many action chunks. The total number of chunks is not a fixed constant: it is an outcome of the rollout under the selected optimization. For the baseline and the two optimization classes, the task completion times are:

$$T^{\text{base}}_{\text{task}} = N^{\text{base}} T_{\text{chunk}}, \quad T^{\text{pl}}_{\text{task}}(\alpha) = N^{\text{pl}}(\alpha) T^{\text{pl}}_{\text{cycle}}(\alpha), \quad T^{\text{ea}}_{\text{task}}(n') = N^{\text{ea}}(n') T^{\text{ea}}_{\text{cycle}}(n'). \tag{4}$$

Here N^{base}, $N^{\text{pl}}(\alpha)$, and $N^{\text{ea}}(n')$ are the total numbers of chunks used by the corresponding rollouts. The end-to-end speedup should compare per-task completion time against the baseline:

$$\eta^{\text{pl}}_{\text{e2e}}(\alpha) = \frac{T^{\text{base}}_{\text{task}}}{T^{\text{pl}}_{\text{task}}(\alpha)} = \frac{N^{\text{base}}}{N^{\text{pl}}(\alpha)} \eta^{\text{pl}}_{\text{chunk}}(\alpha), \quad \eta^{\text{ea}}_{\text{e2e}}(n') = \frac{T^{\text{base}}_{\text{task}}}{T^{\text{ea}}_{\text{task}}(n')} = \frac{N^{\text{base}}}{N^{\text{ea}}(n')} \eta^{\text{ea}}_{\text{chunk}}(n'). \tag{5}$$

$N(\cdot)$ has no closed form, but it grows monotonically as lightweighting strengthens—either via reduced model capacity (under policy-intrinsic compression) or via observation staleness (under execution-aware scheduling). Per-task time therefore need not track per-step time, and may even move in the opposite direction.

> **Overlooked Factor 1**: On static tasks, per-step speedup does not predict per-task speedup—degraded action quality can inflate the chunk count.

Action Delay. We also track the residual action delay, i.e., the time from an observation to the first action that can be executed from the corresponding policy output:

$$D^{\text{base}}_{\text{act}} = T_{\text{inf}}, \quad D^{\text{pl}}_{\text{act}}(\alpha) = \alpha T_{\text{inf}}, \quad D^{\text{ea}}_{\text{act}}(n') = \max\{0, T_{\text{inf}} - n'T_{\text{act}}\}. \tag{6}$$

Dynamic-task analysis further depends on D_{act}, which captures the observation staleness accumulated by the time the corresponding action executes. To cover both policy-intrinsic and execution-aware optimization, let u denote the operating point of the chosen method: $u = \alpha$ for policy-intrinsic

optimization and $u = n'$ for execution-aware optimization. We use a structured surrogate to capture the two dominant factors in dynamic success:

$$\widehat{P}_{\text{succ}}(u) = \Phi(q(u), z(u)), \qquad z(u) = D_{\text{act}}(u)\omega_{\text{env}}, \qquad \partial\Phi/\partial q \geq 0, \qquad \partial\Phi/\partial z \leq 0. \tag{7}$$

where $q(u)$ represents the action quality, ω_{env} is the environment change rate (e.g., conveyor speed or moving-target velocity), $z(u) = D_{\text{act}}(u)\omega_{\text{env}}$ measures how far the environment drifts during the action delay, and Φ maps these two factors to a success rate. In words: dynamic success goes up when actions are more accurate, and goes down when the environment has drifted far from what the policy actually saw. As lightweighting strengthens, $q(u)$ typically falls (less computation or staler input) while $z(u)$ may also fall (faster inference shortens the observation-to-action gap). The outcome for dynamic-task success therefore depends on the relative strength of these two trends.

Overlooked Factor 2: On dynamic tasks, per-step accuracy does not predict per-task accuracy—reduced observation staleness can outweigh the quality loss.

Compute Hardware. The timing terms above are not intrinsic to the policy alone. T_{inf} is determined by the compute platform that runs the policy, whereas T_{act} is fixed by the robot execution side and the task setting. (1) For static tasks, let $\rho = T_{\text{inf}}/T_{\text{act}}$ denote the inference-to-execution time ratio. For a fixed task and a fixed optimization setting, the per-chunk speedups can be written as:

$$\eta^{\text{pl}}_{\text{chunk}}(\rho) = \frac{\rho + n}{\alpha\rho + n}, \quad \eta^{\text{ea}}_{\text{chunk}}(\rho) = \frac{\rho + n}{\rho + n - \min\{\rho, n'\}}. \tag{8}$$

It means that the same lightweighting setting can yield different task-level effects on different compute platforms. (2) For dynamic tasks, the delay D_{act} can also be impacted by hardware ability, thereby affecting $z(u)$ and $\widehat{P}_{\text{succ}}(u)$.

Overlooked Factor 3: Across compute platforms, per-task trends do not generalize—the sweet spot shifts with the hardware's compute budget.

4 Experiments

Section 3 shows that per-step latency is an incomplete proxy for embodied inference optimization. In this section, we empirically characterize how this proxy breaks down through controlled sweeps of lightweighting across task regimes, policy models, optimization methods, and compute platforms. These sweeps are designed to answer three questions: whether per-chunk speedup translates into end-to-end speedup in static tasks, whether reduced action delay translates into better accuracy in dynamic tasks, and whether the shape of the task-level trend and the location of its sweet spot are hardware-dependent. The full experimental combinations, sweep ranges, and implementation details are reported in Appendix B and C.

4.1 Setup

Policy Models. We evaluate policy models at different scales. We use MLP-Mixer [47, 25] and diffusion policy [23] models for simple control tasks, and we also use foundation-scale embodied models in complex environment tasks, including VLAs such as $\pi_{0.5}$ [4] and DynamicVLA [48], and WAMs such as Cosmos-Policy [9] and LingBot-VA [10].

Optimization Methods. For policy-intrinsic optimization, we use quantization, pruning, and sampling-step reduction to accelerate the model inference. To characterize task-level trends with fine granularity, we construct a series of progressively lightweight operating points for each method to adjust α. For execution-aware optimization, we follow the asynchronous inference settings in VLASH [25] and progressively vary the overlap depth n'.

Compute Platforms. We evaluate the latency of policy models' inference on edge devices such as the Jetson AGX Orin [49] (denoted `AGX 15W/30W/50W`) and server-class GPUs, including the RTX 3090 [50] and the Ada 6000 [51]. The power of edge devices can be adjusted to achieve different levels of computational capability.

Config	SR (%)	α	N	T_{chunk}(s)	T_{task}(s)
fp16	64.0	1.00	15.94	0.993	15.83
w8a8	76.0	0.83	16.13	0.961	15.50
w4-t1	66.0	0.82	16.09	0.958	15.42
w4-t2	40.0	0.79	15.85	0.953	15.10
w4-t3	58.0	0.78	15.72	0.951	**14.95**
w4-t4	10.0	0.76	20.20	0.946	19.11
w4-t5	0.0	0.73	N.A.	0.940	N.A.

(a) `Cosmos policy @ Robocasa @ PnP Sink To Counter @ quantization @ Ada 6000`

Config	SR (%)	α	N	T_{chunk}(s)	T_{task}(s)
fp16	100.0	1.00	14.10	0.993	**14.00**
w8a8	100.0	0.83	16.24	0.961	15.61
w4-t1	100.0	0.82	15.88	0.958	15.21
w4-t2	68.0	0.79	18.06	0.953	17.20
w4-t3	70.0	0.78	19.06	0.951	18.12
w4-t4	12.0	0.76	24.00	0.946	22.71
w4-t5	0.0	0.73	N.A.	0.940	N.A.

(b) `Cosmos policy @ Robocasa @ Turn Off Microwave @ quantization @ Ada 6000`

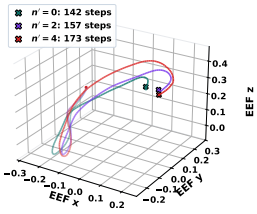

(e) Trajectory

Config	SR (%)	α	N	T_{chunk}(s)	T_{task}(s)
base	90.0	1.00	14.9	2.045	32.19
p1	86.0	0.98	14.9	2.009	31.68
p2	84.0	0.88	15.3	1.820	29.66
p3	76.0	0.88	15.1	1.822	**29.23**
p4	34.0	0.89	22.2	1.838	43.42

(c) `LingBot-VA @ LeRobot @ stack_bowls_3 @ pruning @ Ada 6000`

Config	SR (%)	n'	N	T_{chunk}(s)	T_{task}(s)
d0	93.0	0	51.4	3.255	167.16
d1	94.4	1	49.8	3.222	**160.61**
d2	93.6	2	51.6	3.189	164.43
d3	92.8	3	53.8	3.155	169.80
d4	84.4	4	57.3	3.122	178.89

(d) `pi0.5 @ LIBERO @ 4 task avg @ async @ AGX 50W`

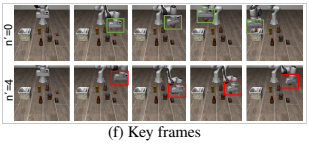

(f) Key frames

Figure 3: Static-task results under `policy model @ task @ sub-task @ optimization method @ hardware` settings. (a)–(d) report SR, optimization strength, N, T_{chunk}, and T_{task}. To avoid interference from timeouts in failed tasks, the reported number N is obtained by averaging over all **successful trials**. For specific configuration details, see Appendix B.1. (e) and (f) visualize the simulation case in (d).

Simulation Task Setup. We evaluate both task regimes defined in Section 3. For static tasks, we use LIBERO [52], RoboCasa [53], and RoboTwin-2.0 [54]. These benchmarks primarily involve manipulation tasks such as grasping and placing stationary objects, where the task-relevant object states remain effectively unchanged during policy inference. For dynamic tasks, we use Kinetix [55] and DOM [48]. These benchmarks' task-relevant states continue to evolve during policy inference, and their latency-injection protocols allow us to emulate different inference delays.

Real-World Task Setup. We further evaluate our observations on a real UR5e robotic arm [56]. In the static setting, the robot needs to pick up a cube on the tabletop and place it in a target box. In the dynamic setting, the robot needs to grasp a cube moving on a conveyor. These two settings share the same manipulation objective but differ in whether the task-relevant object state evolves during policy inference.

4.2 Empirical Finding 1: A Per-Step Speedup Need Not Speed Up the Static Task

As shown in Figure 3, across all four model–task pairs, lightweighting—policy-intrinsic (α) or execution-aware (n')—monotonically reduces the per-chunk time T_{chunk}, but action quality also declines, so the chunk count N grows. Their product $T_{\text{task}} = N \cdot T_{\text{chunk}}$ thus depends on which trend dominates. In Figure 3(a), (c), and (d), N stays nearly flat under mild lightweighting and inflates sharply past a task-specific operating point, so T_{task} traces a U-shape with an interior minimum below the baseline. Figure 3(b) is the corner case: N inflates from the very first optimization step, so no setting beats the baseline. Figure 3(e) and (f) visualize the underlying mechanism on a representative asynchronous trial: as n' grows, the robot arm traces longer end-effector paths and makes more failed grasp attempts before completing the task.

Empirical Finding 1: On static tasks, T_{task} is non-monotonic in lightweighting strength—an interior sweet spot may exist between two regimes: mild lightweighting reduces T_{task} via per-chunk speedup, aggressive lightweighting inflates the chunk count N and reverses the gain.

4.3 Empirical Finding 2: An Imprecise but Faster Reaction Can Improve the Dynamic Task

On dynamic tasks, lightweighting—policy-intrinsic (α) or execution-aware (n')—drives two competing trends: action quality q falls because computation drops, but observation staleness $z = D_{\text{act}}\omega_{\text{env}}$ also falls because the policy reacts on fresher observations. Task success rate P_{succ} thus depends on which trend dominates. Figure 4(a) (Kinetix) shows the regime flip: under the zero-delay assumption (`inf-hw`), accuracy peaks usually at the larger sampling count s; once realistic delay is injected to simulate AGX 15W's inference latency, smaller s becomes the better choice because the reaction-speed gain outweighs the per-step quality loss. Figure 4(b) (DOM-CR) sweeps both s and the environment speed ω_{env}: at every speed, the best configuration is neither the lowest-delay nor the finest-action one, but an interior sweet spot that balances q and z; the sweet-spot location itself shifts with ω_{env}. Figure 4(c) visualizes the paradox in DOM-CR scene.

setting	car	catapult	catcher	grasp	lunar	cheetah
Ideal – zero inference delay						
`inf-hw s1`	0.984	0.555	0.953	0.984	0.914	0.672
`inf-hw s3`	**1.000**	**0.727**	**0.984**	**0.984**	0.914	0.836
`inf-hw s5`	0.992	0.680	0.969	0.953	**0.922**	**0.898**
AGX 15W Simulation– with measured delay						
`agx15 s1 d0`	**0.984**	**0.555**	**0.953**	**0.984**	0.914	0.672
`agx15 s3 d1`	0.938	0.461	0.586	0.844	**0.914**	0.836
`agx15 s5 d2`	0.820	0.477	0.500	0.805	0.867	**0.844**

(a) `MLP-Mixer @ Kinetix`

speed	steps	D_{act}(ms)	SR(%)
100%	1	14.28	68
	2	16.25	**76**
	5	19.92	74
	10	25.69	70
125%	1	14.28	36
	2	16.25	34
	5	19.92	**48**
	10	25.69	46

(b) `DynamicVLA @ DOM-CR`

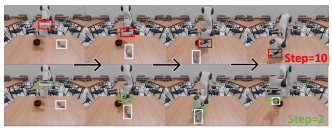

(c) DOM-CR Visualization

Figure 4: (a) Accuracy on Kinetix's 6 sub-tasks. `inf-hw` assumes that policy inference is instantaneous (i.e., zero delay). `s[step]` denotes the number of network iterations. In actual deployment, we measured the policy's inference speed on AGX 15W device and converted its inference delay into an equivalent number of delay steps `d[delay]` in the simulator as shown in Appendix B.2. (b) Accuracy on the DOM-CR sub-task. "speed" indicates the motion speed of objects in the task relative to the original object speed in the dataset. (c) DOM-CR simulator visualization.

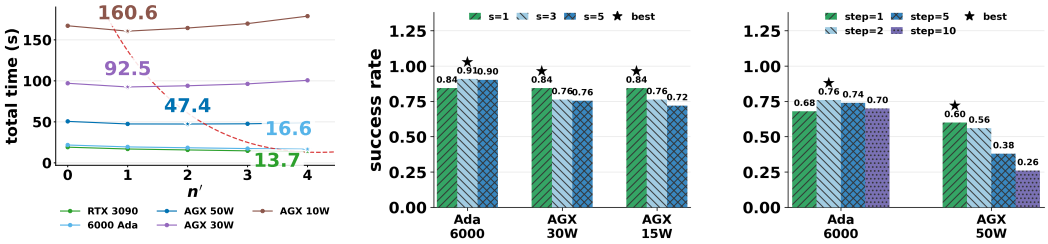

(a) Static task

(b) Dynamic task

Figure 5: (a) On different hardware platforms, the average time required for pi0.5 to complete the LIBERO task versus the asynchronous step n' , with the red dashed line indicating how its sweet spot shifts with hardware; (b) On different hardware platforms, the task accuracy of Kinetix (left) and DOM CR (right) versus the sampling steps, where the location of highest accuracy has shifted.

Empirical Finding 2: On dynamic tasks, task success rate P_{succ} is non-monotonic in lightweighting strength—an interior sweet spot may exist between two regimes: mild lightweighting raises P_{succ} by reducing observation staleness z, aggressive lightweighting collapses action quality q and reverses the gain.

4.4 Empirical Finding 3: The Trend and Optimum Shifts with Hardware

Empirical Findings 1 and 2 established that a sweet spot may exist on both static and dynamic tasks. We next ask whether its location is hardware-dependent. To isolate the hardware effect, we fix the task and the lightweighting sweep, and vary only the inference hardware, which changes the inference-to-execution ratio $\rho = T_{\text{inf}}/T_{\text{act}}$. Figure 5(a) (static, async sweep over n'): on high-performance hardware (ρ small), the per-chunk speedup η_{chunk} is large enough that the gain from inference optimization outweighs the chunk-count inflation, so the sweet spot drifts toward more aggressive overlap; on low-performance hardware (ρ large), the per-chunk gain shrinks while N inflates rapidly, so the sweet spot retreats to milder overlap. Figure 5(b) (dynamic, sampling-step sweep over s): on high-performance hardware, inference delay D_{act} is no longer the dominant factor limiting accuracy, so the sweet spot favors larger s where the policy retains higher action quality q; on low-performance hardware, observation staleness z dominates and the policy must trade off action quality against reaction speed, so the sweet spot shifts to smaller s. Across both regimes, the sweet-spot location is qualitatively sensitive to the hardware compute budget; the quantitative derivation is in Appendix A.2.

Empirical Finding 3: Across compute platforms, the per-task sweet spot shifts with the hardware's compute budget that affects ρ.

4.5 Real-World Experiments

We conduct two real-world studies on a UR5e robot arm as shown in Figure 6. For the static task, we use a fine-tuned $\pi_{0.5}$ model [4] and measure T_{inf} and T_{task} over all successful trials under different sampling-step settings. Table 1a shows that the two metrics exhibit opposite trends as lightweighting becomes more aggressive. For the dynamic experiment, we use a fine-tuned diffusion policy model [23] and compute the score based on the relative position between the gripper and the cube. Table 1c shows that diffusion policies with fewer sampling steps can achieve higher dynamic-task scores, because their faster reaction outweighs the loss in action quality. Tables 1b and 1d further show that the sweet-spot step in both regimes shifts across hardware. Figures 6c and 6d visualize this static-task paradox at the trajectory level: as the sampling step decreases, the grasp-distance trace shows visibly more oscillation. Together, these two real-world studies provide physical evidence for the speedup paradox and corresponding hardware shift.

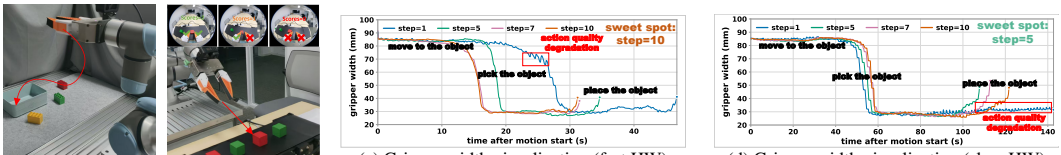

(a) Static setting (b) Dynamic setting (c) Gripper width visualization (fast HW) (d) Gripper width visualization (slow HW)

Figure 6: Real-world experiment visualization on the UR5e platform. (a)(b) Task setups (static pick-and-place; dynamic conveyor grasp). (c)(d) Static-task grasp trajectories under varying step counts with corresponding inference latencies on fast (Ada 6000) and slow (AGX 50W) hardware.

Config	T_{inf}(s)	N	T_{task}(s)	Succ.
step=1	**0.162**	57.4	45.42	5/5
step=7	0.186	49.2	38.74	5/5
step=10	0.199	**47.2**	**37.26**	5/5

(a) Static paradox

HW	s=1	s=5	s=7	s=10
RTX 4070	44.6	41.5	38.6	**37.1**
AGX 50W	159.5	**108.5**	116.9	119.2

(b) Static drift

Config	D_{act}(s)	Pos. 1	Pos. 2	Pos. 3
step=16	0.77	10/20	7/20	9/20
step=4	0.41	**16/20**	**13/20**	**16/20**

(c) Dynamic paradox

HW	s=4	s=16
RTX 4070	48/60	**50/60**
AGX 30W	**45/60**	26/60

(d) Dynamic drift

Table 1: Real-world results on the UR5e platform. (a) Static *paradox* (Empirical Finding 1): faster per-step inference yields slower per-task time (RTX 4070). (b) Static *drift* (Empirical Finding 3): sweet step shifts from 10 (RTX 4070) to 5 (AGX 50W). (c) Dynamic *paradox* (Empirical Finding 2): fewer sampling steps give higher success (AGX 30W). (d) Dynamic *drift* (Empirical Finding 3): sweet step shifts from 16 (RTX 4070) to 4 (AGX 30W).

5 Conclusion

We present TISED, a task-level decomposition framework for analyzing lossy inference optimization in embodied policies. Beyond per-step latency, TISED decomposes optimization into per-chunk speedup, rollout chunk count, action delay, and compute-hardware dependence. Across policy-intrinsic and execution-aware optimization, which validated in both simulation and real-world UR5e experiments, we identify two paradoxes and one drift: (1) faster per-step inference can yield *slower* per-task time on static tasks; (2) less precise inference can yield *higher* success on dynamic tasks; and (3) the per-task sweet spot drifts with the deployment hardware. More fundamentally, these results elevate closed-loop computation to its own design axis, coupling speed, quality, dynamics, and hardware as joint determinants of task-level performance.

6 Limitations

This work has several limitations. (1) Our framework treats per-chunk time and chunk count as the dominant degrees of freedom; second-order effects such as scheduling jitter, and OS-level scheduling latency are abstracted away and may matter for more precise analysis. (2) For execution-aware optimization, we model asynchronous inference as a simplified overlap depth, not as a full server-client implementation; production schedulers may exhibit additional queueing or contention effects. (3) For the static tasks, we approximate N as a function of action quality alone; other effects such as motion jerk and grasp stability is observed but not formally modeled. (4) For the dynamic tasks, extremely high-frequency interactions (e.g., table tennis) are out of scope. (5) Our real-world validation is restricted to a single UR5e platform and two task families; large-scale physical validation is left to future work.

References

[1] M. J. Kim, K. Pertsch, S. Karamcheti, T. Xiao, A. Balakrishna, S. Nair, R. Rafailov, E. Foster, G. Lam, P. Sanketi, et al. Openvla: An open-source vision-language-action model. *arXiv preprint arXiv:2406.09246*, 2024.

[2] M. Shukor, D. Aubakirova, F. Capuano, P. Kooijmans, S. Palma, A. Zouitine, M. Aractingi, C. Pascal, M. Russi, A. Marafioti, et al. Smolvla: A vision-language-action model for affordable and efficient robotics. *arXiv preprint arXiv:2506.01844*, 2025.

[3] K. Black, N. Brown, D. Driess, A. Esmail, M. Equi, C. Finn, N. Fusai, L. Groom, K. Hausman, B. Ichter, et al. π_0: A vision-language-action flow model for general robot control. *arXiv preprint arXiv:2410.24164*, 2024.

[4] K. Black, N. Brown, J. Darpinian, K. Dhabalia, D. Driess, A. Esmail, M. R. Equi, C. Finn, N. Fusai, M. Y. Galliker, et al. $\pi_{0.5}$: a vision-language-action model with open-world generalization. In *9th Annual Conference on Robot Learning*, 2025.

[5] A. Brohan, N. Brown, J. Carbajal, Y. Chebotar, J. Dabis, C. Finn, K. Gopalakrishnan, K. Hausman, A. Herzog, J. Hsu, J. Ibarz, B. Ichter, A. Irpan, T. Jackson, S. Jesmonth, N. J. Joshi, R. Julian, D. Kalashnikov, Y. Kuang, I. Leal, K.-H. Lee, S. Levine, Y. Lu, U. Malla, D. Manjunath, I. Mordatch, O. Nachum, C. Parada, J. Peralta, E. Perez, K. Pertsch, J. Quiambao, K. Rao, M. Ryoo, G. Salazar, P. Sanketi, K. Sayed, J. Singh, S. Sontakke, A. Stone, C. Tan, H. Tran, V. Vanhoucke, S. Vega, Q. Vuong, F. Xia, T. Xiao, P. Xu, S. Xu, T. Yu, and B. Zitkovich. Rt-1: Robotics transformer for real-world control at scale, 2023. URL https://arxiv.org/abs/2212.06817.

[6] A. Brohan, N. Brown, J. Carbajal, Y. Chebotar, X. Chen, K. Choromanski, T. Ding, D. Driess, A. Dubey, C. Finn, P. Florence, C. Fu, M. G. Arenas, K. Gopalakrishnan, K. Han, K. Hausman, A. Herzog, J. Hsu, B. Ichter, A. Irpan, N. Joshi, R. Julian, D. Kalashnikov, Y. Kuang, I. Leal, L. Lee, T.-W. E. Lee, S. Levine, Y. Lu, H. Michalewski, I. Mordatch, K. Pertsch, K. Rao, K. Reymann, M. Ryoo, G. Salazar, P. Sanketi, P. Sermanet, J. Singh, A. Singh, R. Soricut, H. Tran, V. Vanhoucke, Q. Vuong, A. Wahid, S. Welker, P. Wohlhart, J. Wu, F. Xia, T. Xiao, P. Xu, S. Xu, T. Yu, and B. Zitkovich. Rt-2: Vision-language-action models transfer web knowledge to robotic control. In *arXiv preprint arXiv:2307.15818*, 2023.

[7] Octo Model Team, D. Ghosh, H. Walke, K. Pertsch, K. Black, O. Mees, S. Dasari, J. Hejna, C. Xu, J. Luo, T. Kreiman, Y. Tan, L. Y. Chen, P. Sanketi, Q. Vuong, T. Xiao, D. Sadigh, C. Finn, and S. Levine. Octo: An open-source generalist robot policy. In *Proceedings of Robotics: Science and Systems*, Delft, Netherlands, 2024.

[8] S. Liu, L. Wu, B. Li, H. Tan, H. Chen, Z. Wang, K. Xu, H. Su, and J. Zhu. Rdt-1b: a diffusion foundation model for bimanual manipulation. *arXiv preprint arXiv:2410.07864*, 2024.

[9] M. J. Kim, Y. Gao, T.-Y. Lin, Y.-C. Lin, Y. Ge, G. Lam, P. Liang, S. Song, M.-Y. Liu, C. Finn, et al. Cosmos policy: Fine-tuning video models for visuomotor control and planning. *arXiv preprint arXiv:2601.16163*, 2026.

[10] L. Li, Q. Zhang, Y. Luo, S. Yang, R. Wang, F. Han, M. Yu, Z. Gao, N. Xue, X. Zhu, et al. Causal world modeling for robot control. *arXiv preprint arXiv:2601.21998*, 2026.

[11] S. Ye, Y. Ge, K. Zheng, S. Gao, S. Yu, G. Kurian, S. Indupuru, Y. L. Tan, C. Zhu, J. Xiang, A. Malik, K. Lee, W. Liang, N. Ranawaka, J. Gu, Y. Xu, G. Wang, F. Hu, A. Narayan, J. Bjorck, J. Wang, G. Kim, D. Niu, R. Zheng, Y. Xie, J. Wu, Q. Wang, R. Julian, D. Xu, Y. Du, Y. Chebotar, S. Reed, J. Kautz, Y. Zhu, L. J. Fan, and J. Jang. World action models are zero-shot policies, 2026. URL https://arxiv.org/abs/2602.15922.

[12] A. Ye, B. Wang, C. Ni, G. Huang, G. Zhao, H. Li, H. Li, J. Li, J. Lv, J. Liu, M. Cao, P. Li, Q. Deng, W. Mei, X. Wang, X. Chen, X. Zhou, Y. Wang, Y. Chang, Y. Li, Y. Zhou, Y. Ye, Z. Liu, and Z. Zhu. Gigaworld-policy: An efficient action-centered world–action model, 2026. URL https://arxiv.org/abs/2603.17240.

[13] X. Zhai, B. Mustafa, A. Kolesnikov, and L. Beyer. Sigmoid loss for language image pre-training. In *Proceedings of the IEEE/CVF international conference on computer vision*, pages 11975–11986, 2023.

[14] L. Beyer, A. Steiner, A. S. Pinto, A. Kolesnikov, X. Wang, D. Salz, M. Neumann, I. Alabdulmohsin, M. Tschannen, E. Bugliarello, et al. Paligemma: A versatile 3b vlm for transfer. *arXiv preprint arXiv:2407.07726*, 2024.

[15] N. Agarwal, A. Ali, M. Bala, Y. Balaji, E. Barker, T. Cai, P. Chattopadhyay, Y. Chen, Y. Cui, Y. Ding, et al. Cosmos world foundation model platform for physical ai. *arXiv preprint arXiv:2501.03575*, 2025.

[16] D. Hafner, J. Pasukonis, J. Ba, and T. Lillicrap. Mastering diverse domains through world models. *arXiv preprint arXiv:2301.04104*, 2023.

[17] J. Zhang, Y. Hsieh, Z. Wan, H. Lin, X. Wang, Z. Wang, Y. Lei, and M. Zhang. Quantvla: Scale-calibrated post-training quantization for vision-language-action models, 2026. URL https://arxiv.org/abs/2602.20309.

[18] Y. Xu, Y. Yang, Z. Fan, Y. Liu, Y. Li, B. Li, and Z. Zhang. Qvla: Not all channels are equal in vision-language-action model's quantization, 2026. URL https://arxiv.org/abs/2602.03782.

[19] S. Xu, Y. Wang, C. Xia, D. Zhu, T. Huang, and C. Xu. Vla-cache: Efficient vision-language-action manipulation via adaptive token caching. *arXiv preprint arXiv:2502.02175*, 2025.

[20] Y. Li, Y. Meng, Z. Sun, K. Ji, C. Tang, J. Fan, X. Ma, S. Xia, Z. Wang, and W. Zhu. Sp-vla: A joint model scheduling and token pruning approach for vla model acceleration. *arXiv preprint arXiv:2506.12723*, 2025.

[21] H. Wang, J. Xu, Y. Xiang, J. Pan, Y. Zhou, Y.-L. Li, and G. Dai. Specprune-vla: Accelerating vision-language-action models via action-aware self-speculative pruning. *arXiv preprint arXiv:2509.05614*, 2025.

[22] C. Lu, Y. Zhou, F. Bao, J. Chen, C. Li, and J. Zhu. Dpm-solver: A fast ode solver for diffusion probabilistic model sampling in around 10 steps. *arXiv preprint arXiv:2206.00927*, 2022.

[23] C. Chi, Z. Xu, S. Feng, E. Cousineau, Y. Du, B. Burchfiel, R. Tedrake, and S. Song. Diffusion policy: Visuomotor policy learning via action diffusion, 2024. URL https://arxiv.org/abs/2303.04137.

[24] Z. Wang, Z. Li, A. Mandlekar, Z. Xu, J. Fan, Y. Narang, L. Fan, Y. Zhu, Y. Balaji, M. Zhou, M.-Y. Liu, and Y. Zeng. One-step diffusion policy: Fast visuomotor policies via diffusion distillation, 2024. URL https://arxiv.org/abs/2410.21257.

[25] J. Tang, Y. Sun, Y. Zhao, S. Yang, Y. Lin, Z. Zhang, J. Hou, Y. Lu, Z. Liu, and S. Han. Vlash: Real-time vlas via future-state-aware asynchronous inference. *arXiv preprint arXiv:2512.01031*, 2025.

[26] Y. Shi, D. Guo, T. Zhao, F. Gao, L. Shi, C. Yu, Z. Mo, Q. Xiao, X. Peng, Q. Liao, et al. Streamingvla: Streaming vision-language-action model with action flow matching and adaptive early observation. *arXiv preprint arXiv:2603.28565*, 2026.

[27] Y. Lu, Z. Liu, X. Fan, Z. Yang, J. Hou, J. Li, K. Ding, and H. Zhao. Faster: Rethinking real-time flow vlas, 2026. URL https://arxiv.org/abs/2603.19199.

[28] H. Wang, C. Xiong, R. Wang, and X. Chen. Bitvla: 1-bit vision-language-action models for robotics manipulation. 2025.

[29] X. Yan, Z. Wan, F. Ye, X. Yu, H. Du, Y. You, and I. Tsang. Hbvla: Pushing 1-bit post-training quantization for vision-language-action models, 2026. URL https://arxiv.org/abs/2602.13710.

[30] K. Ji, J. Zhou, Y. Meng, Y. Li, H. Cui, and Z. Wang. Sparse actiongen: Accelerating diffusion policy with real-time pruning, 2026. URL https://arxiv.org/abs/2601.12894.

[31] A. Prasad, K. Lin, J. Wu, L. Zhou, and J. Bohg. Consistency policy: Accelerated visuomotor policies via consistency distillation, 2024. URL https://arxiv.org/abs/2405.07503.

[32] M. Clemente, L. Brunswic, R. H. Yang, X. Zhao, Y. Khalil, H. Lei, A. Rasouli, and Y. Li. Two-steps diffusion policy for robotic manipulation via genetic denoising, 2025. URL https://arxiv.org/abs/2510.21991.

[33] S. Li, L. Sun, and Y. Chen. One-step flow policy: Self-distillation for fast visuomotor policies, 2026. URL https://arxiv.org/abs/2603.12480.

[34] K. Zhou, Q. Chen, D. Peng, Z. Li, X. Li, and J. Gu. Characterizing vision-language-action models across xpus: Constraints and acceleration for on-robot deployment, 2026. URL https://arxiv.org/abs/2604.24447.

[35] S. Han, H. Mao, and W. J. Dally. Deep compression: Compressing deep neural networks with pruning, trained quantization and huffman coding. *arXiv preprint arXiv:1510.00149*, 2015.

[36] A. G. Howard, M. Zhu, B. Chen, D. Kalenichenko, W. Wang, T. Weyand, M. Andreetto, and H. Adam. Mobilenets: Efficient convolutional neural networks for mobile vision applications, 2017. URL https://arxiv.org/abs/1704.04861.

[37] G. Xiao, J. Lin, M. Seznec, H. Wu, J. Demouth, and S. Han. SmoothQuant: Accurate and efficient post-training quantization for large language models. In *Proceedings of the 40th International Conference on Machine Learning*, 2023.

[38] J. Lin, J. Tang, H. Tang, S. Yang, W.-M. Chen, W.-C. Wang, G. Xiao, X. Dang, C. Gan, and S. Han. Awq: Activation-aware weight quantization for llm compression and acceleration. In *MLSys*, 2024.

[39] T. Liang, J. Glossner, L. Wang, S. Shi, and X. Zhang. Pruning and quantization for deep neural network acceleration: A survey, 2021. URL https://arxiv.org/abs/2101.09671.

[40] X. Zhu, J. Li, Y. Liu, C. Ma, and W. Wang. A survey on model compression for large language models, 2024. URL https://arxiv.org/abs/2308.07633.

[41] M. Li, Y. Wang, and D. Ramanan. Towards streaming perception. In *ECCV*, 2020.

[42] H. Kang, Q. Zhang, H. Cai, W. Xu, T. Krishna, Y. Du, and T. Weissman. Win fast or lose slow: Balancing speed and accuracy in latency-sensitive decisions of llms. *Advances in Neural Information Processing Systems*, 38:150862–150884, 2026.

[43] W. Jiang, J. Clemons, K. Sankaralingam, and C. Kozyrakis. How fast can i run my vla? demystifying vla inference performance with vla-perf, 2026. URL https://arxiv.org/abs/2602.18397.

[44] A. Taherin, J. Lin, A. Akbari, A. Akbari, P. Zhao, W. Chen, D. Kaeli, and Y. Wang. Cross-platform scaling of vision-language-action models from edge to cloud gpus, 2026. URL https://arxiv.org/abs/2509.11480.

[45] Z. Li, H. Yang, Z. Chen, Y. Chen, C. Li, et al. From inference efficiency to embodied efficiency: Revisiting efficiency metrics for vision-language-action models. *arXiv preprint arXiv:2603.19131*, 2026.

[46] T. Z. Zhao, V. Kumar, S. Levine, and C. Finn. Learning fine-grained bimanual manipulation with low-cost hardware. *arXiv preprint arXiv:2304.13705*, 2023.

[47] I. Tolstikhin, N. Houlsby, A. Kolesnikov, L. Beyer, X. Zhai, T. Unterthiner, J. Yung, A. Steiner, D. Keysers, J. Uszkoreit, M. Lucic, and A. Dosovitskiy. Mlp-mixer: An all-mlp architecture for vision, 2021. URL https://arxiv.org/abs/2105.01601.

[48] H. Xie, B. Wen, J. Zheng, Z. Chen, F. Hong, H. Diao, and Z. Liu. Dynamicvla: A vision-language-action model for dynamic object manipulation. *arXiv preprint arXiv:2601.22153*, 2026.

[49] NVIDIA Jetson AGX Orin — nvidia.com. https://www.nvidia.com/en-us/autonomous-machines/embedded-systems/jetson-orin/, .

[50] 3090 & 3090 Ti Graphics Cards — nvidia.com. https://www.nvidia.com/en-us/geforce/graphics-cards/30-series/rtx-3090/, .

[51] NVIDIA RTX 6000 Ada Generation Graphics Card — nvidia.com. https://www.nvidia.com/en-us/products/workstations/rtx-6000/, .

[52] B. Liu, Y. Zhu, C. Gao, Y. Feng, Q. Liu, Y. Zhu, and P. Stone. Libero: Benchmarking knowledge transfer for lifelong robot learning. *arXiv preprint arXiv:2306.03310*, 2023.

[53] S. Nasiriany, A. Maddukuri, L. Zhang, A. Parikh, A. Lo, A. Joshi, A. Mandlekar, and Y. Zhu. Robocasa: Large-scale simulation of everyday tasks for generalist robots. In *Robotics: Science and Systems (RSS)*, 2024.

[54] T. Chen, Z. Chen, B. Chen, Z. Cai, Y. Liu, Z. Li, Q. Liang, X. Lin, Y. Ge, Z. Gu, W. Deng, Y. Guo, T. Nian, X. Xie, Q. Chen, K. Su, T. Xu, G. Liu, M. Hu, H.-a. Gao, K. Wang, Z. Liang, Y. Qin, X. Yang, P. Luo, and Y. Mu. Robotwin 2.0: A scalable data generator and benchmark with strong domain randomization for robust bimanual robotic manipulation. *arXiv preprint arXiv:2506.18088*, 2025.

[55] M. Matthews, M. Beukman, C. Lu, and J. Foerster. Kinetix: Investigating the training of general agents through open-ended physics-based control tasks. 2025. URL https://arxiv.org/abs/2410.23208.

[56] e-Series Robots — universal-robots.com. https://www.universal-robots.com/products/e-series/.

[57] S. Ashkboos, A. Mohtashami, M. L. Croci, B. Li, P. Cameron, M. Jaggi, D. Alistarh, T. Hoefler, and J. Hensman. Quarot: Outlier-free 4-bit inference in rotated llms, 2024. URL https://arxiv.org/abs/2404.00456.

[58] R. Cadene, S. Alibert, F. Capuano, M. Aractingi, A. Zouitine, P. Kooijmans, J. Choghari, M. Russi, C. Pascal, S. Palma, M. Shukor, J. Moss, A. Soare, D. Aubakirova, Q. Lhoest, Q. Gallouédec, and T. Wolf. Lerobot: An open-source library for end-to-end robot learning. In *The Fourteenth International Conference on Learning Representations*, 2026. URL https://arxiv.org/abs/2602.22818.

[59] C. Chi, Z. Xu, C. Pan, E. Cousineau, B. Burchfiel, S. Feng, R. Tedrake, and S. Song. Universal manipulation interface: In-the-wild robot teaching without in-the-wild robots, 2024. URL https://arxiv.org/abs/2402.10329.

[60] E. J. Hu, Y. Shen, P. Wallis, Z. Allen-Zhu, Y. Li, S. Wang, L. Wang, and W. Chen. Lora: Low-rank adaptation of large language models, 2021. URL https://arxiv.org/abs/2106.09685.

[61] A. Radford, J. W. Kim, C. Hallacy, A. Ramesh, G. Goh, S. Agarwal, G. Sastry, A. Askell, P. Mishkin, J. Clark, G. Krueger, and I. Sutskever. Learning transferable visual models from natural language supervision, 2021. URL https://arxiv.org/abs/2103.00020.

[62] A. Dosovitskiy, L. Beyer, A. Kolesnikov, D. Weissenborn, X. Zhai, T. Unterthiner, M. Dehghani, M. Minderer, G. Heigold, S. Gelly, J. Uszkoreit, and N. Houlsby. An image is worth 16x16 words: Transformers for image recognition at scale, 2021. URL https://arxiv.org/abs/2010.11929.

Contents

A Detailed Analysis of the TISED (Section 3) **15**

A.1 When Does a "Sweet Spot" Exist? 15

A.2 How Does the "Sweet Spot" Move with Hardware? 17

A.3 Assumptions and Limitations 18

B Simulation Experiment Details (Section 4.2, 4.3, 4.4) **18**

B.1 Optimization Method Settings 18

B.2 Task Settings 20

B.3 Result Visualization 21

C Real-World Experiment Details (Section 4.5) **22**

C.1 Static Experiment Settings 22

C.2 Dynamic Experiment Settings 23

D Additional Discussions **23**

D.1 About "Successful-Only Trial's Chunks" 23

D.2 Stability and Motion Smoothness 23

A Detailed Analysis of the TISED (Section 3)

This section provides a quantitative interpretation of the task-level inference speedup effect decomposition (TISED) introduced in the main paper. Table 2 summarizes the notation used in the derivation.

Symbol	Meaning	Symbol	Meaning
h	Compute hardware platform.	ρ_h	Ratio $T_{\mathrm{inf},h}/T_{\mathrm{act}}$.
α	Policy-intrinsic inference-time ratio, with $\alpha \in [\alpha_{\min}, 1]$.	n'	Discrete asynchronous overlap depth, with $n' \in \{0, \ldots, n\}$.
$\alpha_{\min}$	Smallest α whose policy accuracy remains above zero.		
$T_{\mathrm{inf},h}$	Baseline inference time on h.	T_{act}	Execution time of one atomic action.
n	Actions in one chunk.	$T^{\mathrm{base}}_{\mathrm{chunk},h}$	Baseline action-chunk time.
$T^{\mathrm{pl/ea}}_{\mathrm{chunk},h}$	Optimized per-chunk time.	$N^{\mathrm{pl/ea}}$	Chunks required for task completion.
$T^{\mathrm{pl/ea}}_{\mathrm{task},h}$	End-to-end completion time.	$D^{\mathrm{pl/ea}}_{\mathrm{act},h}$	Observation-to-action delay.
q	Action quality.	ω_{env}	Environment evolution rate.
z_h	Staleness exposure $D_{\mathrm{act},h}\omega_{\mathrm{env}}$.	Φ	Task response function.
$P_{\mathrm{succ},h}$	Modeled dynamic-task success rate.		

Table 2: Notation used in the quantitative analysis of the TISED framework.

A.1 When Does a "Sweet Spot" Exist?

A.1.1 Optimization Variables

Policy-Intrinsic Optimization. We analyze the inference-time ratio $\alpha \in [\alpha_{\min}, 1]$, where smaller α means more aggressive lightweighting. All derivatives with respect to α below are therefore taken in the direction of *less* aggressive lightweighting. When reading the same result along the optimization-strength direction used in the plots, the direction is reversed.

Execution-Aware Optimization. We analyze the overlap depth $n' \in \{0, \ldots, n\}$, where larger n' means more aggressive overlap between inference and action execution.

A.1.2 Static Tasks

Policy-Intrinsic Optimization. For static tasks, we have

$$T^{\mathrm{pl}}_{\mathrm{task},h}(\alpha) = N^{\mathrm{pl}}(\alpha) T^{\mathrm{pl}}_{\mathrm{chunk},h}(\alpha), \qquad T^{\mathrm{pl}}_{\mathrm{chunk},h}(\alpha) = \alpha T_{\mathrm{inf},h} + n T_{\mathrm{act}}. \tag{9}$$

Increasing α means moving toward a more conservative policy: action quality improves and the required chunk count decreases, i.e., $\mathrm{d}N^{\mathrm{pl}}(\alpha)/\mathrm{d}\alpha < 0$, but each chunk becomes slower. These two monotone effects act in opposite directions on $T^{\mathrm{pl}}_{\mathrm{task},h} = N^{\mathrm{pl}} T^{\mathrm{pl}}_{\mathrm{chunk},h}$: mild lightweighting can be dominated by the per-chunk speedup, whereas aggressive lightweighting can be dominated by the growth of N^{pl}. The derivative of $T^{\mathrm{pl}}_{\mathrm{task,h}}$ with respect to α can be written as a competition between the cost of slower chunks and the benefit of requiring fewer chunks:

$$\frac{\mathrm{d}T^{\mathrm{pl}}_{\mathrm{task},h}(\alpha)}{\mathrm{d}\alpha} = \underbrace{N^{\mathrm{pl}}(\alpha) T_{\mathrm{inf},h}}_{\text{cost: slower chunks}} - \underbrace{\left[-\frac{\mathrm{d}N^{\mathrm{pl}}(\alpha)}{\mathrm{d}\alpha}\right](\alpha T_{\mathrm{inf},h} + n T_{\mathrm{act}})}_{\text{benefit: fewer chunks}}. \tag{10}$$

An interior minimum occurs only when the derivative of the task time changes sign:

$$\left.\frac{\mathrm{d}T^{\mathrm{pl}}_{\mathrm{task},h}(\alpha)}{\mathrm{d}\alpha}\right|_{\alpha=\alpha_{\min}} < 0, \qquad \left.\frac{\mathrm{d}T^{\mathrm{pl}}_{\mathrm{task},h}(\alpha)}{\mathrm{d}\alpha}\right|_{\alpha=1} > 0. \tag{11}$$

Otherwise, the shortest T_{task} setting can lie at one endpoint.

Execution-Aware Optimization. For execution-aware optimization, the corresponding objective is

$$T^{\mathrm{ea}}_{\mathrm{task},h}(n') = N^{\mathrm{ea}}(n')T^{\mathrm{ea}}_{\mathrm{chunk},h}(n'), \qquad T^{\mathrm{ea}}_{\mathrm{chunk},h}(n') = T_{\mathrm{inf},h} + nT_{\mathrm{act}} - \min\{T_{\mathrm{inf},h}, n'T_{\mathrm{act}}\}\,. \tag{12}$$

Larger n' means more aggressive overlap. Increasing n' can reduce $T^{\mathrm{ea}}_{\mathrm{chunk},h}$ by hiding more inference behind action execution, but excessive overlap may increase N^{ea} because action quality or observation–execution alignment degrades. Let $\Delta f(n') = f(n'+1) - f(n')$; then

$$\begin{aligned}\Delta T^{\mathrm{ea}}_{\mathrm{task},h}(n') &= T^{\mathrm{ea}}_{\mathrm{task},h}(n'+1) - T^{\mathrm{ea}}_{\mathrm{task},h}(n') \\ &= \underbrace{\Delta N^{\mathrm{ea}}(n')T^{\mathrm{ea}}_{\mathrm{chunk},h}(n'+1)}_{\text{cost: more chunks}} - \underbrace{N^{\mathrm{ea}}(n')\left[-\Delta T^{\mathrm{ea}}_{\mathrm{chunk},h}(n')\right]}_{\text{benefit: faster chunks}}\,.\end{aligned} \tag{13}$$

An interior discrete sweet spot appears when the first overlap step improves completion time but excessive overlap later hurts:

$$\Delta T^{\mathrm{ea}}_{\mathrm{task},h}(0) < 0, \qquad \Delta T^{\mathrm{ea}}_{\mathrm{task},h}(n-1) > 0. \tag{14}$$

Otherwise, the shortest T_{task} setting can lie at one endpoint.

A.1.3 Dynamic Tasks

Policy-Intrinsic Optimization. We model the policy-intrinsic dynamic-task success rate as

$$P^{\mathrm{pl}}_{\mathrm{succ},h}(\alpha) \approx \Phi\Big(q^{\mathrm{pl}}(\alpha), z^{\mathrm{pl}}_h(\alpha)\Big)\,, \qquad z^{\mathrm{pl}}_h(\alpha) = D^{\mathrm{pl}}_{\mathrm{act},h}(\alpha)\omega_{\mathrm{env}} = \alpha T_{\mathrm{inf},h}\omega_{\mathrm{env}}. \tag{15}$$

Here Φ is assumed to be monotone in the two arguments:

$$\Phi_q = \frac{\partial \Phi}{\partial q} \geq 0, \qquad \Phi_z = \frac{\partial \Phi}{\partial z} \leq 0,$$

meaning that better action quality increases the modeled success rate, while larger staleness exposure decreases it. Increasing α usually improves action quality but also increases action delay: $\mathrm{d}q^{\mathrm{pl}}(\alpha)/\mathrm{d}\alpha \geq 0$ and $\mathrm{d}z^{\mathrm{pl}}_h(\alpha)/\mathrm{d}\alpha = T_{\mathrm{inf},h}\omega_{\mathrm{env}} > 0$. Thus, differentiating the surrogate response gives

$$\frac{\mathrm{d}P^{\mathrm{pl}}_{\mathrm{succ},h}(\alpha)}{\mathrm{d}\alpha} \approx \underbrace{\Phi_q \frac{\mathrm{d}q^{\mathrm{pl}}(\alpha)}{\mathrm{d}\alpha}}_{\text{benefit: better action quality}} - \underbrace{\left[-\Phi_z\right] T_{\mathrm{inf},h}\omega_{\mathrm{env}}}_{\text{cost: larger action delay}}\,. \tag{16}$$

An interior dynamic-task sweet spot appears when this trade-off creates a sign change:

$$\left.\frac{\mathrm{d}P^{\mathrm{pl}}_{\mathrm{succ},h}}{\mathrm{d}\alpha}\right|_{\alpha=\alpha_{\min}} > 0, \qquad \left.\frac{\mathrm{d}P^{\mathrm{pl}}_{\mathrm{succ},h}}{\mathrm{d}\alpha}\right|_{\alpha=1} < 0. \tag{17}$$

Otherwise, the best P_{succ} setting can lie at one of the endpoints.

Execution-Aware Optimization. The same response model becomes

$$P^{\mathrm{ea}}_{\mathrm{succ},h}(n') \approx \Phi(q^{\mathrm{ea}}(n'), z^{\mathrm{ea}}_h(n'))\,, \qquad z^{\mathrm{ea}}_h(n') = \max\{0, T_{\mathrm{inf},h} - n'T_{\mathrm{act}}\}\omega_{\mathrm{env}}. \tag{18}$$

Increasing n' means more aggressive execution-aware optimization. It can reduce staleness exposure by hiding inference behind action execution, but it may also degrade action quality or observation–execution alignment. Let $\Delta f(n') = f(n'+1) - f(n')$. Then $\Delta z^{\mathrm{ea}}_h(n') \leq 0$ before overlap saturation, while $\Delta q^{\mathrm{ea}}(n')$ can be negative when deeper overlap hurts action quality. A first-order finite-difference approximation gives

$$\Delta P^{\mathrm{ea}}_{\mathrm{succ},h}(n') \approx \underbrace{\left[-\Phi_z\right]\left[-\Delta z^{\mathrm{ea}}_h(n')\right]}_{\text{benefit: smaller action delay}} - \underbrace{\Phi_q\left[-\Delta q^{\mathrm{ea}}(n')\right]}_{\text{cost: degraded action quality}}\,. \tag{19}$$

The corresponding discrete condition for an interior dynamic-task sweet spot is

$$\Delta P^{\mathrm{ea}}_{\mathrm{succ},h}(0) > 0, \qquad \Delta P^{\mathrm{ea}}_{\mathrm{succ},h}(n-1) < 0. \tag{20}$$

Otherwise, the best P_{succ} setting can lie at one endpoint.

A.2 How Does the "Sweet Spot" Move with Hardware?

A.2.1 Static Tasks: Take Execution-Aware Optimization as Example

We assume $N^{\mathrm{ea}}(n'+1) \geq N^{\mathrm{ea}}(n')$. The hardware-dependent sweet spot is

$$(n')_h^\star \in \arg\min_{n' \in \{0,\ldots,n\}} N^{\mathrm{ea}}(n')\left(\rho_h + n - \min(\rho_h, n')\right). \tag{21}$$

For a local interpretation, suppose a reference hardware h_0 with ρ_0 has an old sweet spot $(n')_0^\star$. If $(n')_0^\star$ lies in the unsaturated branch, i.e., $(n')_0^\star < \rho_0$, then

$$T_{\mathrm{task}}^{\mathrm{ea}}(n';\rho) = T_{\mathrm{act}} N^{\mathrm{ea}}(n')(\rho + n - n'). \tag{22}$$

The complete derivative with respect to n' and the reference sweet-spot condition are

$$\begin{aligned} \frac{\partial T_{\mathrm{task}}^{\mathrm{ea}}}{\partial n'} &= T_{\mathrm{act}}\left[\frac{\mathrm{d}N^{\mathrm{ea}}(n')}{\mathrm{d}n'}(\rho + n - n') - N^{\mathrm{ea}}(n')\right], \\ \left.\frac{\partial T_{\mathrm{task}}^{\mathrm{ea}}}{\partial n'}\right|_{n'=(n')_0^\star,\rho=\rho_0} &= T_{\mathrm{act}}\left[\frac{\mathrm{d}N^{\mathrm{ea}}(n')}{\mathrm{d}n'}(\rho_0 + n - n') - N^{\mathrm{ea}}(n')\right]\Bigg|_{n'=(n')_0^\star} = 0. \end{aligned} \tag{23}$$

Evaluating the slope at the same old setting after changing hardware to ρ_1 gives

$$\left.\frac{\partial T_{\mathrm{task}}^{\mathrm{ea}}}{\partial n'}\right|_{n'=(n')_0^\star,\rho=\rho_1} = T_{\mathrm{act}}(\rho_1 - \rho_0)\left.\frac{\mathrm{d}N^{\mathrm{ea}}(n')}{\mathrm{d}n'}\right|_{n'=(n')_0^\star}. \tag{24}$$

We have $\frac{\mathrm{d}N^{\mathrm{ea}}(n')}{\mathrm{d}n'} \geq 0$, corresponding to $N^{\mathrm{ea}}(n'+1) - N^{\mathrm{ea}}(n') \geq 0$ in the finite sweep. Thus, in the unsaturated branch, slower compute hardware with $\rho_1 > \rho_0$ gives a positive local slope at the old sweet spot, so the relaxed optimum tends to move toward smaller n'.

If the new hardware places the setting in the saturated branch, i.e., $n' \geq \rho_1$, the per-chunk time becomes $T_{\mathrm{chunk}}^{\mathrm{ea}} = nT_{\mathrm{act}}$ and no longer decreases with deeper overlap. Under $\frac{\mathrm{d}N^{\mathrm{ea}}}{\mathrm{d}n'} \geq 0$, increasing n' in this branch can only keep or increase $T_{\mathrm{task}}^{\mathrm{ea}}$.

A.2.2 Dynamic Tasks: Take Policy-Intrinsic Optimization as Example

For the measured policy-intrinsic sweep,

$$\alpha_h^\star \in \arg\max_{\alpha_i \in \mathcal{A}} \Phi\Big(q_i^{\mathrm{pl}}, \alpha_i \rho_h T_{\mathrm{act}} \omega_{\mathrm{env}}\Big), \tag{25}$$

where q_i^{pl} denotes the measured or induced action quality at setting α_i. Suppose a reference hardware h_0 with ρ_0 has an interior dynamic sweet spot $\alpha_0^\star$, we have

$$P_{\mathrm{succ}}^{\mathrm{pl}}(\alpha;\rho) \approx \Phi\big(q^{\mathrm{pl}}(\alpha), \alpha\rho T_{\mathrm{act}}\omega_{\mathrm{env}}\big), \tag{26}$$

Let $z^{\mathrm{pl}}(\alpha,\rho) = \alpha\rho T_{\mathrm{act}}\omega_{\mathrm{env}}$. The complete derivative with respect to α is

$$\frac{\partial P_{\mathrm{succ}}^{\mathrm{pl}}}{\partial \alpha} = \Phi_q\big(q^{\mathrm{pl}}(\alpha), z^{\mathrm{pl}}(\alpha,\rho)\big)\frac{\mathrm{d}q^{\mathrm{pl}}(\alpha)}{\mathrm{d}\alpha} + \Phi_z\big(q^{\mathrm{pl}}(\alpha), z^{\mathrm{pl}}(\alpha,\rho)\big)\rho T_{\mathrm{act}}\omega_{\mathrm{env}}, \tag{27}$$

where Φ_q and Φ_z denote the partial derivatives of Φ with respect to action quality and normalized staleness, respectively. The reference sweet spot therefore satisfies

$$\left[\Phi_q \frac{\mathrm{d}q^{\mathrm{pl}}}{\mathrm{d}\alpha} + \Phi_z \rho_0 T_{\mathrm{act}}\omega_{\mathrm{env}}\right]_{\alpha=\alpha_0^\star,\rho=\rho_0} = 0. \tag{28}$$

Ignoring higher-order sensitivity changes of Φ, the local slope after changing hardware to ρ_1 becomes

$$\left.\frac{\partial P_{\mathrm{succ}}^{\mathrm{pl}}}{\partial \alpha}\right|_{\alpha=\alpha_0^\star,\rho=\rho_1} \approx (\rho_1 - \rho_0)T_{\mathrm{act}}\omega_{\mathrm{env}}\ \Phi_z|_{\alpha=\alpha_0^\star,\rho=\rho_0}. \tag{29}$$

Here $z = \alpha\rho T_{\mathrm{act}}\omega_{\mathrm{env}}$ denotes normalized staleness, and $\Phi_z \leq 0$ means that larger staleness lowers success. Therefore, a slower compute platform with $\rho_1 > \rho_0$ makes the old sweet spot have a negative local slope, so the maximizer tends to move toward smaller α, i.e., a lower-delay but potentially lower-quality policy setting.

A.3 Assumptions and Limitations

The analysis above is intentionally structured but lightweight. The analysis above makes several idealized assumptions. First, quantities such as $N^{\mathrm{pl}}(\alpha)$ and $N^{\mathrm{ea}}(n')$ are specified only through their qualitative trends. Their concrete functional forms are task-dependent and must be obtained from empirical measurement. Second, Φ is used only as an abstract response function that describes how dynamic-task success depends on action quality and action delay. We do not assume that Φ has a fixed parametric form or represents a calibrated physical law.

B Simulation Experiment Details (Section 4.2, 4.3, 4.4)

This section describes how we design the optimization methods and choose the task regimes.

B.1 Optimization Method Settings

We summarize the policy models used in the main paper and their corresponding static and dynamic evaluation configurations in Tables 3 and 4.

Model	Task and optimization method	Default action-generation steps	n	Action freq. (Hz)	T_{exec} (ms)	nT_{exec} (ms)
Cosmos-Policy	LIBERO & Asynchronous Inference; RoboCasa & Quantization	1	16	20	50.0	800.0
LingBot-VA	RoboTwin & Pruning	10	2	16.7	60.0	120.0
$\pi_{0.5}$	LIBERO & Asynchronous Inference	10	5	30	33.3	166.7

Table 3: Simulation static-task configurations.

Model	Task and optimization method	Default refinement-steps
MLP-Mixer	Kinetix & flow-style refinement-step reduction	5
DynamicVLA	DOM-CR & flow-matching refinement-step reduction	10

Table 4: Simulation dynamic-task configurations.

Quantization. At the operator level, we replace the FP16 linear layers in Transformer-based policies with integer linear operators, including int4-weight/int4-activation (W4A4) and int8-weight/int8-activation (W8A8) variants. The additional quantization and dequantization operators are fused into the surrounding operators to reduce inference overhead. We do not apply extra transformations such as smoothing [37] or rotation [57]. To obtain fine-grained operating points and expose potential sweet spots, we construct a progressive tier-10 quantization sweep as in [42]; the Cosmos-Policy quantization configurations are listed in Table 5.

Pruning. For the pruning sweep, we use LingBot-VA [10] on RoboTwin tasks and implement a KV-cache pruning method. In the default RoboTwin setting, `attn_window=72`, which allocates up to 36 historical visual-latent chunks and 36 historical action chunks in the baseline cache. Our pruning further shortens the readable window inside this native cache. Let $\mathcal{C}^{\mathrm{vis}}_{<t}$ and $\mathcal{C}^{\mathrm{act}}_{<t}$ denote the valid visual-latent and action KV slots retained by the native attention window before step t. The pruned attention reads only

$$\mathcal{R}_t = \mathrm{Recent}_{W_{\mathrm{lat}}}\left(\mathcal{C}^{\mathrm{vis}}_{<t}\right) \cup \mathrm{Recent}_{W_{\mathrm{act}}}\left(\mathcal{C}^{\mathrm{act}}_{<t}\right), \qquad h_t = \mathrm{Attn}(q_t, K_{\mathcal{R}_t}, V_{\mathcal{R}_t}), \tag{30}$$

where $\mathrm{Recent}_W(\cdot)$ keeps the most recent W slots of the corresponding cache stream. Figure 7 illustrates the difference between the native-window baseline and our read-window pruning. The pruned setting keeps cache writing unchanged but exposes only the most recent W_{lat} and W_{act} entries to attention.

Table 6 lists the operating points used in the sweep. To make the pruning strength directly comparable across settings, we first report the total readable KV budget retained relative to the baseline.

Main label	Speedup vs. FP16	W4A4 sites	Remaining higher-precision sites
fp16	1.00×	None	All candidate sites remain FP16.
w8a8	1.33×	None	All candidate sites use W8A8.

w4-t1	1.36×	`ca.out@late`	W8A8:
			`ca.out@early/mid`
			`sa.*@all`
			`ca.q/k/v@all`
			`mlp.l1/l2@all`

w4-t2	1.41×	`ca.out@late`
		`mlp.l1@early`
			W8A8:
			`ca.out@early/mid`
			`mlp.l1@mid/late`
			`sa.*@all`
			`ca.q/k/v@all`
			`mlp.l2@all`

w4-t3	1.42×	`ca.out@early/late`
		`mlp.l1@early`
			W8A8:
			`ca.out@mid`
			`mlp.l1@mid/late`
			`sa.*@all`
			`ca.q/k/v@all`
			`mlp.l2@all`

w4-t4	1.47×	`ca.out@early/late`
		`mlp.l1@early/late`
			W8A8:
			`ca.out@mid`
			`mlp.l1@mid`
			`sa.*@all`
			`ca.q/k/v@all`
			`mlp.l2@all`

w4-t5	1.53×	`ca.out@early/late`
		`mlp.l1@all`
			W8A8:
			`ca.out@mid`
			`sa.*@all`
			`ca.q/k/v@all`
			`mlp.l2@all`

w4-t6	1.55×	`ca.out@all`
		`mlp.l1@all`
			W8A8:
			`sa.*@all`
			`ca.q/k/v@all`
			`mlp.l2@all`

w4-t7	1.67×	`ca.out@all`
		`mlp.l1/l2@all`
			W8A8:
			`sa.*@all`
			`ca.q/k/v@all`

w4-t8	1.88×	`ca.out@all`
		`mlp.l1/l2@all`
		`sa.q/k/out@all`
			W8A8:
			`sa.v@all`
			`ca.q/k/v@all`

w4-t9	2.05×	`sa.q/k/v/out@all`
		`ca.q/out@all`
		`mlp.l1/l2@all`
			W8A8:
			`ca.k/v@all`

w4-t10	2.09×	`sa.q/k/v/out@all`
		`ca.q/k/v/out@all`
		`mlp.l1/l2@all`
			None; all candidate sites use W4A4.

Table 5: Mapping between the quantization shorthand and the progressive tier-10 Cosmos-Policy quantization settings. Speedup is measured from LIBERO 5-step latency profiling relative to all-FP16. The sweep starts from all-W8A8 and progressively converts selected DiT attention/MLP linear sites to W4A4. Here, `early/mid/late` denote DiT blocks `B0--B9/B10--B19/B20--B27`; `sa`, `ca`, and `mlp` denote self-attention, cross-attention, and feed-forward MLP sites; `q/k/v/out` denote attention projections, and `l1/l2` denote the two MLP linear layers.

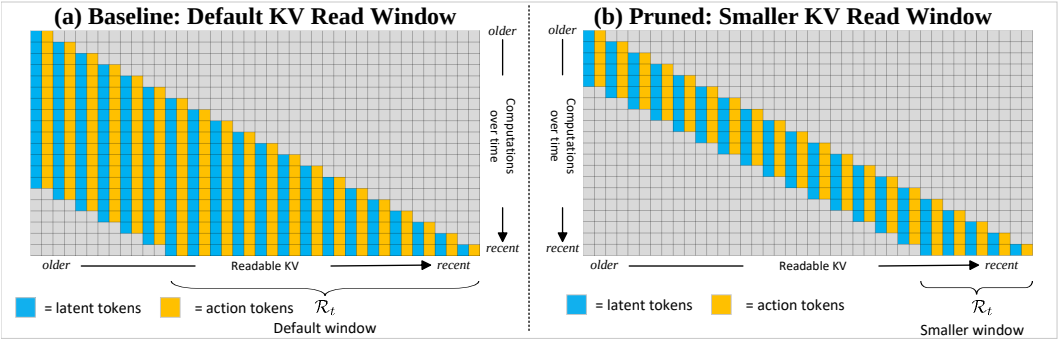

Figure 7: KV-cache read-window pruning for LingBot-VA. The baseline attends to all valid visual-latent and action KV slots retained by the native attention window. The pruned setting further restricts attention to the most recent readable cache windows, while the cache-writing path remains unchanged.

Config	Readable KV Compression Ratio	Visual KV budget	Action KV budget	Visual hist. chunks	Action hist. chunks
base	100.0%	8640	1152	36.0	36.0
p1	13.1%	1024	256	4.3	8.0
p2	6.5%	512	128	2.1	4.0
p3	3.3%	256	64	1.1	2.0
p4	1.6%	128	32	0.5	1.0

Table 6: LingBot-VA KV-cache read-window configurations. The "readable KV Compression Ratio" column reports the total readable KV Compression Ratio, visual plus action, normalized by the baseline, so smaller values indicate more aggressive lightweighting. Baseline are determined by the native attention window, and pruning reduces only the readable KV budget inside that window.

This normalized value decreases monotonically from `base` to `p4`, so smaller values indicate more aggressive lightweighting. The KV-budget columns then report the maximum number of readable historical tokens for the visual-latent and action streams. The chunk columns convert these token budgets using the RoboTwin configuration. Each visual-latent chunk contains 240 KV tokens, and each action chunk contains 32 KV tokens. For example, $1024/256$ means that each action-generation step can read at most the most recent 1024 visual-latent KV entries and 256 action KV entries, corresponding to roughly 4.3 visual chunks and 8 action chunks.

Action-Generation Step-Count Reduction. We reduce the number of action-generation steps used to generate each action chunk. We then evaluate a progressive step sweep to characterize the trade-off between computing speed and action quality.

Asynchronous Inference. We adopt the simplified asynchronous-inference model from VLASH [25]. The overlap depth between inference and execution is controlled by n': at simulation step t, the policy receives the stale observation from $t - n'$ steps earlier. This emulates delayed machine-vision input due to overlapping policy inference and action execution.

B.2 Task Settings

We group the simulation benchmarks according to the task regimes defined in the main paper: LIBERO, RoboCasa, and the LeRobot(RoboTwin) tasks are used as static-task benchmarks, while Kinetix and DOM-CR are used as dynamic-task benchmarks.

LIBERO. LIBERO [52] is a tabletop manipulation benchmark suite designed to evaluate policy generalization and knowledge transfer across object, spatial, goal, and long-horizon task variations. We use it as a controlled static-task setting because the task-relevant object and goal states are assumed to remain unchanged during policy inference.

RoboCasa. RoboCasa [53] provides large-scale simulated household manipulation tasks with diverse kitchen layouts, objects, and task instances. Despite the static-scene assumption, RoboCasa tasks are typically more challenging than those in LIBERO.

LeRobot. LeRobot [58] is an open-source robot-learning ecosystem that standardizes datasets, policy training, and evaluation interfaces across simulated and real manipulation tasks. For LingBot-VA, the data and evaluation interface follow the LeRobot-style format, while the underlying simulated environments are generated from RoboTwin [54], a SAPIEN-based dual-arm manipulation benchmark with multi-camera observations and diverse bimanual tasks. These tasks are treated as static manipulation tasks because task-relevant objects do not deliberately move during policy inference.

Kinetix. Kinetix [55] is a 2D physics-based control benchmark with procedurally designed tasks involving contact-rich interaction, object manipulation, locomotion, balance, and timing-sensitive control. The policy is an iterative, flow-style action generator with an MLP-Mixer architecture [25], and we vary the number of refinement steps in $\{1, 3, 5\}$ to trade off zero-delay action quality against inference latency. We evaluate both zero-delay inference, denoted as `inf-hw` in the main text, and hardware-induced delay. For the latter, we profile inference latency τ and map it to an integer control-step delay $d = \mathrm{round}(\tau/33.33\mathrm{ms})$, since Kinetix applies actions every two 16.67 ms physics steps. Consequently, different profiled latencies can fall into the same simulator delay bin.

Execution setting	Steps	τ (ms)	d	Effective delay (ms)
Ada 6000	1	1.80	0	0.00
Ada 6000	3	3.81	0	0.00
Ada 6000	5	9.82	0	0.00
AGX 30W	1	7.78	0	0.00
AGX 30W	3	21.44	1	33.33
AGX 30W	5	35.80	1	33.33
AGX 15W	1	7.78	0	0.00
AGX 15W	3	33.75	1	33.33
AGX 15W	5	54.63	2	66.67

Table 7: Kinetix latency-to-delay configuration.

DOM. The Dynamic Object Manipulation (DOM) benchmark is introduced with DynamicVLA [48] to evaluate policies on moving-object manipulation, where the environment continues to evolve during inference delay. It organizes dynamic scenarios along three dimensions: interaction, perception, and generalization. We focus on Closed-loop Reactivity (CR), a sub-dimension of interaction that evaluates how quickly a policy adjusts to objects moving at different speeds. We vary the action expert's refinement steps in $\{1, 2, 5, 10\}$ and inject simulator delays calibrated to emulate inference latency on different hardware platforms. We evaluate object-motion speed scales of 100% and 125% relative to the original dataset. For each combination of object speed, refinement-step setting, and latency condition, we run 50 trials and report the task success rate and action delay.

B.3 Result Visualization

Figure 8 replots the four static-task tables in Section 4.2 as line charts. All three quantities are normalized by the corresponding baseline value in each panel. The star marks the operating point with the lowest T_{task}.

Notably, the variation trends manifest differently across different tasks. For example, for the pick-and-place sink-to-counter task in Figure 8(a), N remains roughly stable through moderate quantization, so the latency reduction dominates and the shortest per-task time appears at `w4-t3`. For the turn-off-microwave task in Figure 8(b), N increases quickly even under mild quantization, so the full-precision baseline remains the shortest end-to-end time.

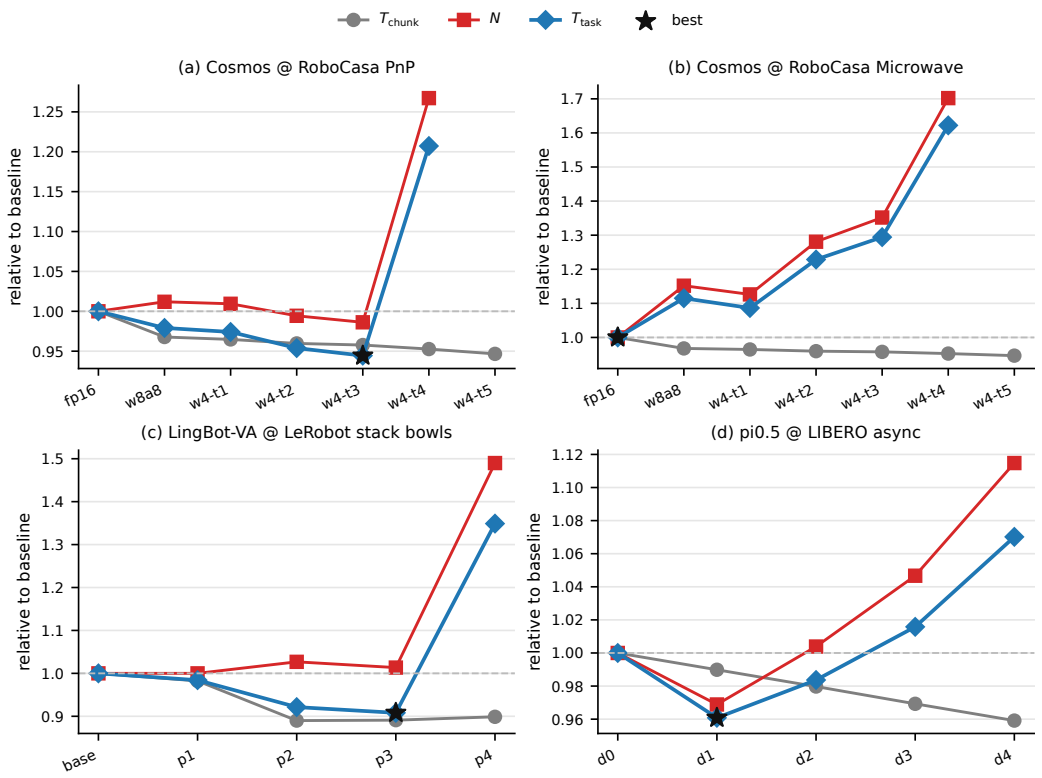

Figure 8: Visualization of the static-task measurements reported in Section 4.2. Values are normalized within each panel by the baseline configuration. In (a), (c), and (d), mild optimization reduces T_{task}, while more aggressive settings eventually increase the required chunk count N enough to reverse the gain, producing an interior sweet spot. In (b), the baseline is already the best measured point, showing that such a sweet spot is not guaranteed and its existence and location are task-dependent.

C Real-World Experiment Details (Section 4.5)

We use a UR5e robot arm [56] to validate the two task regimes in the physical world. The real-world robot setup follows UMI [59], with the mirrors on the gripper removed. The setup consists of a UR5e robot arm, a UMI gripper, and a GoPro camera for RGB observation. All experiments were conducted with the same robot arm speed setting of 30% and a control frequency of 10 Hz.

To evaluate how compute capability, i.e., ρ, affects T_{task} or task accuracy, we first profile the policy model's inference latency T_{inf} across different hardware platforms. We then introduce a hardware-latency scaling factor λ on the RTX 4070 platform, i.e., $T_{\text{task,simulated}} = \lambda T_{\text{task,original}}, \rho_{\text{simulated}} = \lambda \rho_{\text{original}}$, which allows us to simulate the inference behavior of different compute platforms under the same task environment.

C.1 Static Experiment Settings

We collected 198 expert demonstrations using the UMI gripper and fine-tuned the $\pi_{0.5}$ [4] model for 30,000 training steps using LoRA [60]. During LoRA fine-tuning, we initialized the policy from the $\pi_{0.5}$-base model, which consists of two components: a VLM backbone and an action expert. The VLM backbone is PaliGemma [14], composed of a SigLIP vision encoder and a Gemma-2B language model, while the action expert is a 300M Gemma model. We fine-tuned both components with a learning rate of 2.5×10^{-5} and a batch size of 32.

The static manipulation task requires the robot to pick up a red cube on the tabletop and place it into a target box. A trial is considered successful only if the gripper fingers open and release the cube

into the target box. Each rollout started from the same predefined initial position. For each rollout setting, we conducted 5 trials and reported the corresponding task performance.

C.2 Dynamic Experiment Settings

We collected 196 expert demonstrations using the UMI gripper and trained the diffusion policy [23] for 130 epochs. The diffusion policy model is composed of a pretrained ViT vision encoder and a DiT action decoder. The DiT module was trained from scratch with a learning rate of 3.0×10^{-4}. For the visual encoder, we initialized the ViT backbone from the CLIP [61] pretrained ViT-L/14 model [62] and trained it with a learning rate of 3.0×10^{-5} and a batch size of 32.

The dynamic manipulation task requires the robot to grasp the red cube as it moves on a conveyor. We evaluate grasping performance using a three-level score: 2 indicates that the red cube is successfully grasped and held by both gripper fingers; 1 indicates that only one gripper finger contacts the red cube; and 0 indicates that neither gripper finger reaches the red cube. This scoring criterion reports both the robot's reaction speed and motion quality in the dynamic task. The conveyor moved at a constant speed of 6.25 cm/s during evaluation. For each rollout setting, we conducted 30 trials. Specifically, we used three fixed initial positions and performed 10 trials for each position.

D Additional Discussions

D.1 About "Successful-Only Trial's Chunks"

Following the successful-episode reporting protocol in prior work [45], we report chunk number and completion time only over successful rollouts:

$$N_{\text{succ}} = \mathbb{E}[N \mid \text{success}], \qquad T_{\text{task,succ}} = \mathbb{E}[T_{\text{task}} \mid \text{success}]. \tag{31}$$

The successful-only convention avoids an artifact of simulator rollouts: when a task fails, the simulator may continue executing additional chunks and corrective attempts until the rollout horizon is reached. Including timeout trajectories would inflate N and T_{task}, so the averages would reflect the simulator termination rule instead of the efficiency of completed executions.

D.2 Stability and Motion Smoothness

Prior work [45] analyzed in simulation several embodied-efficiency indicators that deteriorate as the degree of lightweighting increases, such as jerk. We additionally conduct real-world experiments on the UR5e platform.

For an end-effector trajectory $\mathbf{x}_0, \ldots, \mathbf{x}_{K-1}$ sampled at interval Δt, we quantify motion jerk as

$$\widehat{J} = \frac{1}{K-3} \sum_{k=0}^{K-4} \left\| \frac{\mathbf{x}_{k+3} - 3\mathbf{x}_{k+2} + 3\mathbf{x}_{k+1} - \mathbf{x}_k}{\Delta t^3} \right\|_2^2. \tag{32}$$

We report $\widehat{J}$ over static task trials for each step setting in Table 8. The result shows that stronger lightweighting leads to larger motion jerk in real-world execution. This result is consistent with the simulator observation in work [45], indicating that aggressive lightweighting can reduce the policy model's computation while degrading physical motion quality.

Table 8: Real-world jerk under different step settings.

Steps	1	5	7	10
$\widehat{J}$ ($\mathrm{m}^2/\mathrm{s}^6$)	0.512	0.334	0.313	0.283